

www.acsaem.org Article

Atomic-Level Understanding of Surface Reconstruction Based on $Li[Ni_xMn_yCo_{1-x-y}]O_2$ Single-Crystal Studies

Jian Zhu, Soroosh Sharifi-Asl, Juan C. Garcia, Hakim H. Iddir, Jason R. Croy, Reza Shahbazian-Yassar, and Guoying Chen*



Cite This: ACS Appl. Energy Mater. 2020, 3, 4799–4811



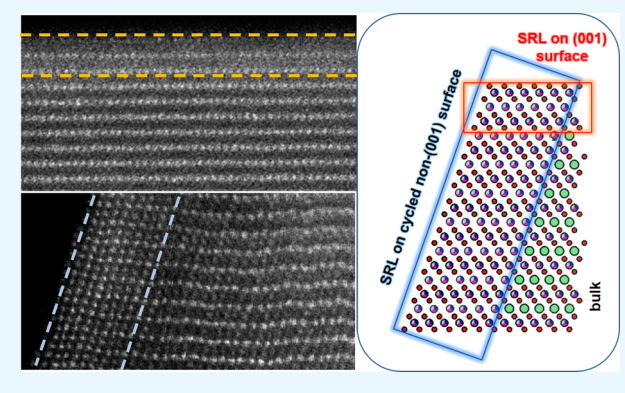
ACCESS

III Metrics & More

Article Recommendations

Supporting Information

ABSTRACT: The stability of cathode particle surfaces that are directly exposed to the electrolyte is one of the most crucial and determining factors for cathode performance at high operating voltages. Theory has predicted a strong dependence of surface stability on chemical compositions as well as surface facets of layered oxides, yet conflicting results on the correlations exist as most experimental studies focus on cycled secondary particles recovered from composite electrodes. Herein, we synthesize well-formed $\text{Li}[\text{Ni}_x \text{Mn}_y \text{Co}_{1-x-y}] \text{O}_2$ (NMC) single-crystal samples, carefully define pristine surface properties, and then monitor their evolution with cycling. Atomicresolution scanning transmission electron microscopy (STEM) imaging and electron energy loss spectroscopy (EELS) analysis show the formation of a surface reconstruction layer (SRL) as well as an



extended surface reduction layer on pristine, Li-permeable non-(001) surfaces, even before cycling. We reveal a transition region with chemical gradient, in which the layered structure gradually densifies and eventually transforms into the SRL on the top surface. Contrary to these observations, no SRL is observed on pristine, Li-impermeable (001) surfaces, revealing the facet-dependent nature of surface reconstructions during particle synthesis. Upon electrochemical cycling, significant composition- and facet-dependent SRL growth is observed. The driving force and mechanism for surface reconstruction are further discussed. The present study provides insights into the origin as well as the nature of SRLs, highlighting the significance of surface engineering in cathode material optimization.

KEYWORDS: Li-ion battery cathodes, Li[Ni_xMn_yCo_{1-x-y}]O₂ (NMC), surface reconstruction, single crystals, surface face dependent, composition dependent

1. INTRODUCTION

Because of their high practical volumetric energy densities, Nirich layered transition-metal (TM) oxides (TMOs) such as $\text{Li}[\text{Ni}_x \text{Mn}_y \text{Co}_{1-x-y}] \text{O}_2$ (NMCs, x > 0.5) are considered as one of the most promising cathode materials for next-generation lithium-ion batteries (LIBs). However, several performance issues, such as capacity fade, impedance rise, and thermal instability, become significantly worse with increasing Ni content. It is known that layered-to-spinel-to-rocksalt phase transformations take place on the surface of cycled NMCs, a phenomenon that is exacerbated as Ni contents increase. The formation of such SRLs may block the transport of Li ions and electrons, consequently leading to impedance rise as well as capacity and energy losses. The design of better performing surfaces, therefore, is of great importance to improved cyclability of Ni-rich NMCs, especially under high-voltage/ state-of-charge (SOC) operating conditions.

Extensive effort has been dedicated to the study of surface stability against reconstruction in TMOs, including NMCs, lithium nickel cobalt aluminum oxides (NCAs), and lithium-

and manganese-rich transition-metal oxides (LMRs). In most studies, the process that leads to surface reconstruction is considered universal on all surfaces, although only certain surface facets, generally those that are not parallel to $\{003\}$ planes, were studied. ^{11–15} It is only in recent years that local anisotropic surface reconstructions have been taken into consideration. For example, anisotropic surface reconstruction of LiNi_{0.4}Mn_{0.4}Co_{0.18}TiO_{0.02}O₂ was observed along the Li diffusion direction after only one cycle between 2.0 and 4.7 V. ¹⁶ In a study of the impact of electrolyte additives and upper cutoff voltage on LiNi_{0.8}Mn_{0.1}Co_{0.1}O₂ (NMC811), SRLs were found only on surfaces not parallel to the TM slabs (e.g., surfaces with open Li channels), regardless of the electrolyte

Received: February 26, 2020 Accepted: April 30, 2020 Published: April 30, 2020





additives or upper cutoff voltages used. 17 A two-stage rocksalt formation and growth mechanism was revealed on Ni-rich NMC materials after prolonged cycling, including (1) formation of uniform surface reconstruction layer of ~2 nm and (2) anisotropic growth of the rocksalt phase into the bulk along {104} planes controlled by the solid-liquid interface or electrolyte chemistry. 18 Previous studies on LMRs suggest that the pristine surfaces of primary particles terminated with alternating TM-O-Li slabs tend to have thicker SRLs, but no apparent facet dependence was found on primary particles postcycling. 19–23 Work on pristine NCA particles reported more severe surface reconstruction on the Li-impermeable (003) surface due to the formation of a rocksalt phase via the interlayer mixing of Li/TM.²⁴ All aforementioned studies were performed on secondary particles. As controlling primaryparticle size, shape, and composition uniformity in a secondary particle is inherently difficult, there is a lack of overall understanding on the relationship among anisotropic reconstruction, composition, and surface facet. Furthermore, we recently performed detailed STEM/EELS studies to evaluate the behavior of individual primary particles within secondary particles.²⁵ It was found that primary particles in the core of the secondary particle experience less surface reconstruction, partly because they are shielded from the contact with the electrolyte. This suggests the likelihood of misinterpretation when primary particles from secondary particles are examined. By use of well-formed crystal samples in our study, potential impact from built-in microstructures is excluded, and all particles can be expected to experience a similar level of charge and discharge.

In this study, we synthesize well-formed single crystalline NMC particles with dominating (001) family facets (in platelet morphology) and investigate composition- and facet-dependent surface reconstruction before and after electrochemical cycling. LiNi_{0.33}Mn_{0.33}Co_{0.33}O₂ (NMC333) and LiNi_{0.6}Mn_{0.2}- $Co_{0.2}O_{2}$ (NMC622) single crystals with the same platelet morphology were used to illustrate the changes in the SRL as a function of Ni content and surface facet. SRL formation was characterized via atomic-resolution STEM imaging, EELS, and synchrotron X-ray absorption spectroscopy (XAS). We found SRLs present on pristine, non-(001) surfaces terminated by alternating TM-O-Li layers, whereas no SRLs were found on pristine (001) surfaces terminated by TM slabs. In addition, higher Ni content was associated with more severe surface reconstruction of pristine particles. Cycling-induced SRL growth was broadly observed, which also showed compositionand facet-dependent behavior. The mechanism for surface reconstruction in both pristine and cycled NMCs is discussed.

2. EXPERIMENTAL SECTION

2.1. Synthesis. The pristine NMC crystal samples were prepared via a two-step process: preparation of TM hydroxide precursors by the coprecipitation method followed by annealing them with lithium hydroxide. In a typical process, stoichiometric amounts of NiSO₄· $6H_2O$, MnSO₄· H_2O , and CoSO₄· $7H_2O$ (Sigma-Aldrich, >99%), together with 0.5 g of polyvinylpyrrolidone (PVP, with an average $M_w = 1300000$), were dissolved in distilled water to obtain a TM sulfate solution A (0.8 M). NaOH and ammonia were dissolved in distilled water to prepare a solution B, at a concentration of 2.0 and 0.2 M, respectively. Solutions A and B were added dropwise to 1 M ammonia aqueous solution under stirring for 20 h. The pH of the mixed solution was maintained at 11–12. The resulting precipitate was filtered and washed with distilled water and ethanol several times to remove dissolved salts. The washed particles were dried in a

vacuum oven at 60 °C overnight. The as-obtained transition-metal hydroxide precursor was then mixed with LiOH·H $_2$ O (with 6 mol % excess to compensate Li loss at high temperature) and annealed together for 10 h at 850 and 800 °C for NMC333 and NMC622, respectively.

2.2. Characterization. Powder X-ray diffraction (PXRD) was performed by using a Bruker D2 powder X-ray diffractometer (λ (Cu $K\alpha$) = 0.15418 nm, 40 kV, 30 mA). Chemical compositions of NMC samples were determined by using inductively coupled plasma optical emission spectrometry (ICP-OES, PerkinElmer Optima 5300 DV). Field emission scanning electron microscope (FESEM) imaging was performed by using a JEOL JSM-7500F field emission scanning electron microscope at an accelerating voltage of 15 kV. Hard X-ray absorption spectroscopy (hXAS) spectra of Ni, Mn, and Co K-edges were collected in transmission mode by using a (220) monochromator at the Stanford Synchrotron Radiation Light source (SSRL) beamline 2-2. Pristine and cycled NMCs, recovered from cycled electrodes, were sandwiched between two pieces of Kapton tape in an argon-filled glovebox for the hXAS measurements. The Si (220) monochromator was detuned (~20%?) for each element before the measurement to reduce the harmonics in the X-ray beam. Energy calibration was performed by setting the first inflection points in the spectra of Ni, Mn, and Co metal foil references to 8333, 6539, and 7709 eV, respectively. X-ray absorption near-edge structure (XANES) spectra were processed by using SIXPACK software (Sam's Interface for XAS Package developed by Sam Webb at SSRL, the Stanford Synchrotron Radiation Laboratory). Soft XAS (sXAS) spectra were collected at SSRL on the 31-pole wiggler beamline 10-1 in a single load at ambient temperature under ultrahigh vacuum (10⁻⁹ Torr) by using the total electron yield (TEY) and the fluorescence yield (FY) mode detectors. A ring current of 350 mA, a 1000 lines mm⁻¹ spherical grating monochromator with 40 μ m entrance and exit slits, a 0.2 eV energy resolution, and a 1 mm² beam spot were used. A thin layer of pristine powder sample, or a small piece of recovered electrode, was loaded onto conductive carbon tape on an aluminum sample bar in an argon-filled glovebox for sXAS measurement. sXAS spectra data were processed by using the PyMca software.²⁶

Aberration-corrected scanning transmission electron microscopy (AC-STEM) was performed by using a JEOL JEM-ARM200CF STEM equipped with a cold field emission gun with 0.78 Å spatial resolution. Atomic resolution images were obtained by a high-angle annular dark-field (HAADF) detector with a 90 mrad inner-detector angle and a 22 mrad probe convergence angle. Electron energy loss spectroscopy (EELS) was performed by using a Gatan Quantum detector. EELS results were obtained with 0.5 eV/channel dispersion and a 5 mm detector aperture. The full width at half-maximum of zero loss peak was measured 1.8 eV, which determines the energy resolution of the obtained spectra. Energy dispersive spectroscopy (EDS) results were obtained by an Oxford X-max 100TLE windowless X-ray detector in the range 0–10 keV. Sample preparation was done by dispersing the cathode particles in methanol and dropcasting the solution onto a 300-mesh carbon-coated copper grid and drying in air.

2.3. Electrochemical Testing. To prepare the NMC composite electrodes, a slurry consisting of pristine NMC crystals, acetylene black conductive additive, and poly(vinylidene fluoride) (PVDF) binder in a weight ratio of 8:1:1 in N-methylpyrrolidone (NMP) solvent was prepared. The slurry was then coated onto a carboncoated aluminum foil current collector (Exopack Advanced Coatings) and dried under vacuum at 120 $^{\circ}\text{C}$ overnight. Cathode discs with an area of 1.6 cm² and an active mass loading of ~3 mg/cm² were cut from the coated electrode sheets. The electrode discs were galvanostatically cycled in 2032-type coin cells with lithium metal (Alfa-Aesar) counter and reference electrodes, a Celgard 2325 membrane separator, and a GEN 2 electrolyte containing 1.2 M LiPF₆ in ethylene carbonate (EC)/ethyl methyl carbonate (EMC) (3:7 weight ratio, Novolyte Technologies Inc.). Electrochemical measurements were performed at ambient temperature on a VMP3 multichannel potentiostat/galvanostat, controlled by EC-lab software (BioLogic Science Instruments), at a rate of C/10. Postcycling, NMC

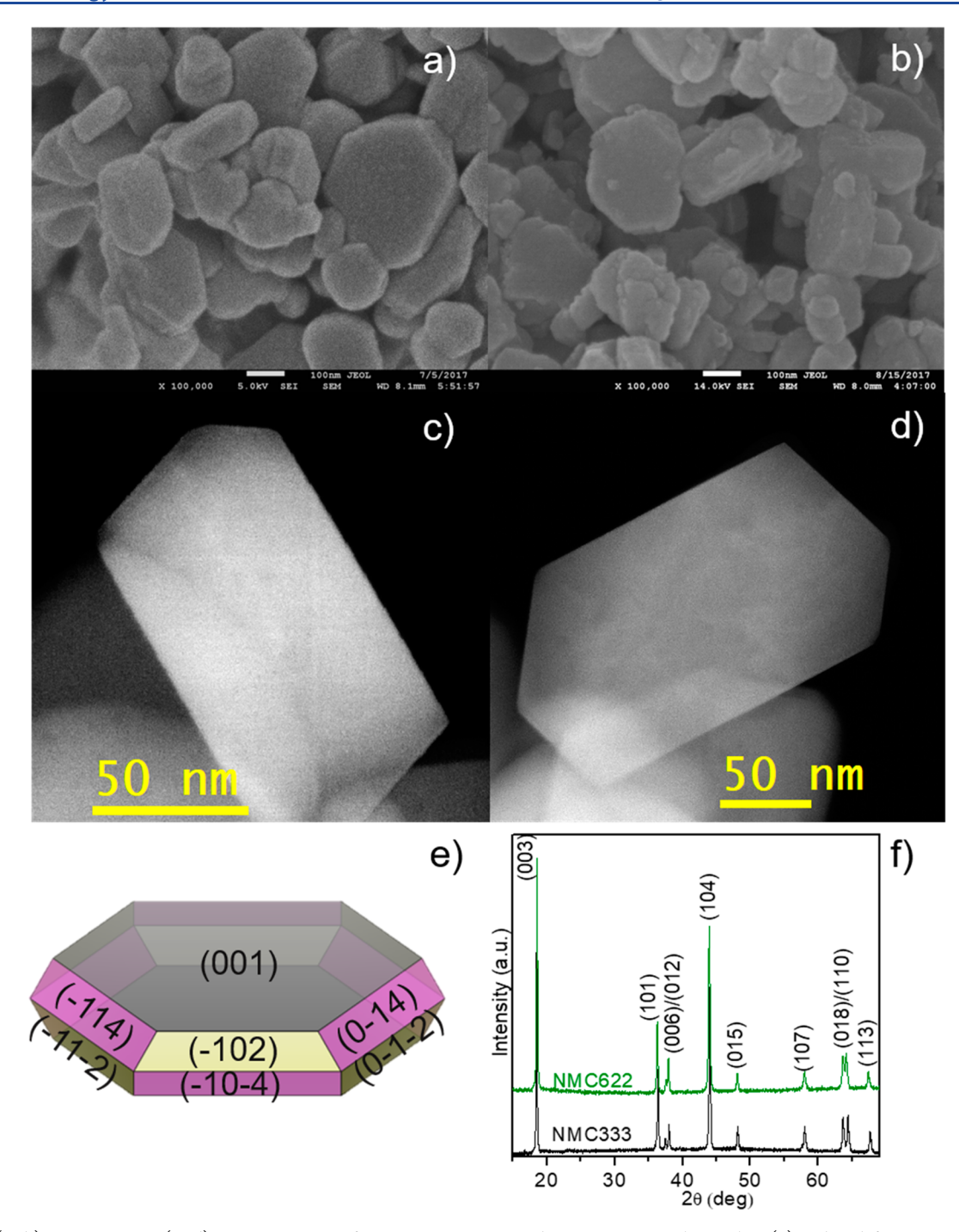


Figure 1. (a, b) SEM images, (c, d) STEM images of pristine NMC333 and NMC622 crystal samples, (e) indexed facets on platelet NMC particles, and (f) XRD patterns of pristine NMC333 and NMC622 crystal samples.

electrodes were recovered from the cells and rinsed with dimethyl carbonate (DMC) before the post-mortem analysis.

3. RESULTS AND DISCUSSION

3.1. NMC Bulk Structure. The discrete platelet-shaped NMC333 and NMC622 crystal samples were obtained by using a two-step process: coprecipitation of TM sulfate precursors followed by annealing of the resulting intermediate with lithium hydroxide. A small amount of PVP, which is a surfactant commonly used as a surface stabilizer, a growth modifier, or nanoparticle dispersant in various reactions, ²⁷ was added during the coprecipitation process to influence the

nucleation speed and crystal growth. The as-synthesized NMC samples had an average platelet size of ~200 nm and a thickness of ~50 nm, as shown in Figures 1a and 1b for NMC333 and NMC622, respectively. This was further confirmed by STEM imaging, where the platelet morphology with sharp edges of well-defined facets is clearly seen on both samples (Figures 1c and 1d). EDX elemental mapping revealed a uniform distribution of the TM cations and oxygen anions at the particle level (Figures S1a and S1b for NMC333 and NMC622, respectively), which is in clear contrast to the heterogeneity often seen in conventional secondary particles with built-in grain boundaries.²⁰ By use of the same TEM and

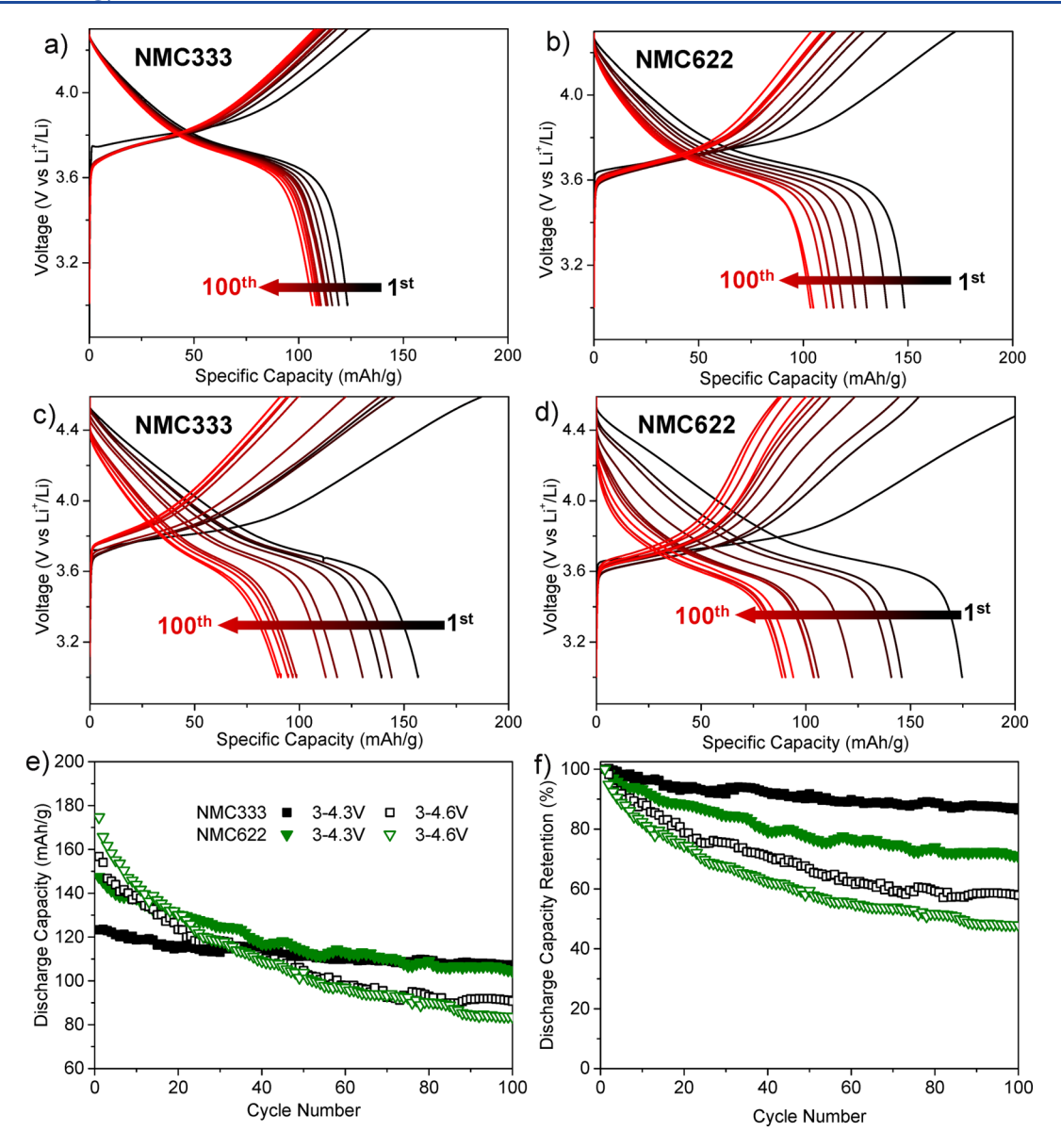


Figure 2. First 100-cycle charge—discharge profiles of (a, c) NMC333 and (b, d) NMC622 in the voltage window of (a, b) 3–4.3 V and (c, d) 3–4.6 V. (e) and (f) show the comparison of discharge capacity and capacity retention at a cycling rate of C/10, respectively.

selected area electron diffraction (SAED) analysis procedures reported in our previous studies, ²⁸ the single crystal nature of the samples was confirmed after verifying the single crystalline orientation throughout the particles.

Previous DFT calculations demonstrated that in layered LiTMO₂ (TM = transition metals) such as LiCoO₂, NMC333, and NMC811 the thermodynamically equilibrated particle shapes are enclosed by three dominant families of surface facets, namely (104), (001), and (012).^{29–31} While the (001) plane is parallel with the Li and TM slabs in the crystal structure and is Li ion impermeable, both (012) and (104) facets are terminated with alternating TM-O-Li slabs and therefore Li-permeable (Figure S2). Among them, the surface energies of the (012) and (104) facets are the highest and lowest, respectively. The crystalline planes exposed on the particle surface were index by using the shape analysis technique reported in a recent publication.³² For both NMC333 and NMC622, more than 85% of the platelet

surface is covered by the (001) facets (Figure 1e), consistent with the previous results.

The XRD patterns collected on the as-synthesized NMC333 and NMC622 samples (Figure 1f) confirm that both samples are phase pure with the hexagonal α -NaFeO₂ structure ($R\overline{3}m$ space group). Clear peak splitting in the (006)/(012) and (018)/(110) doublets were observed, confirming the wellordered layered structure.³³ The width of the splits narrows with increasing Ni content from NMC333 to NMC622, likely due to an increase in cation mixing in the latter due to the size similarity between Ni²⁺ (0.69 Å) and Li⁺ (0.76 Å), as reported in the previous studies.³⁴ Rietveld refinement of the XRD patterns are shown in Figure S3, and the refined parameters are listed in Table S1. The lattice parameters for NMC333 are a =b = 2.8937 (1) Å and c = 14.3476 (3) Å, with a c/a ratio of 4.96. These parameters are slightly decreased in NMC622, with a = b = 2.8782 (1) Å and c = 14.2481 (2) Å and with a c/a ratio of 4.95. These values are similar to what was reported in the literature. 35-41 The nominal composition determined by

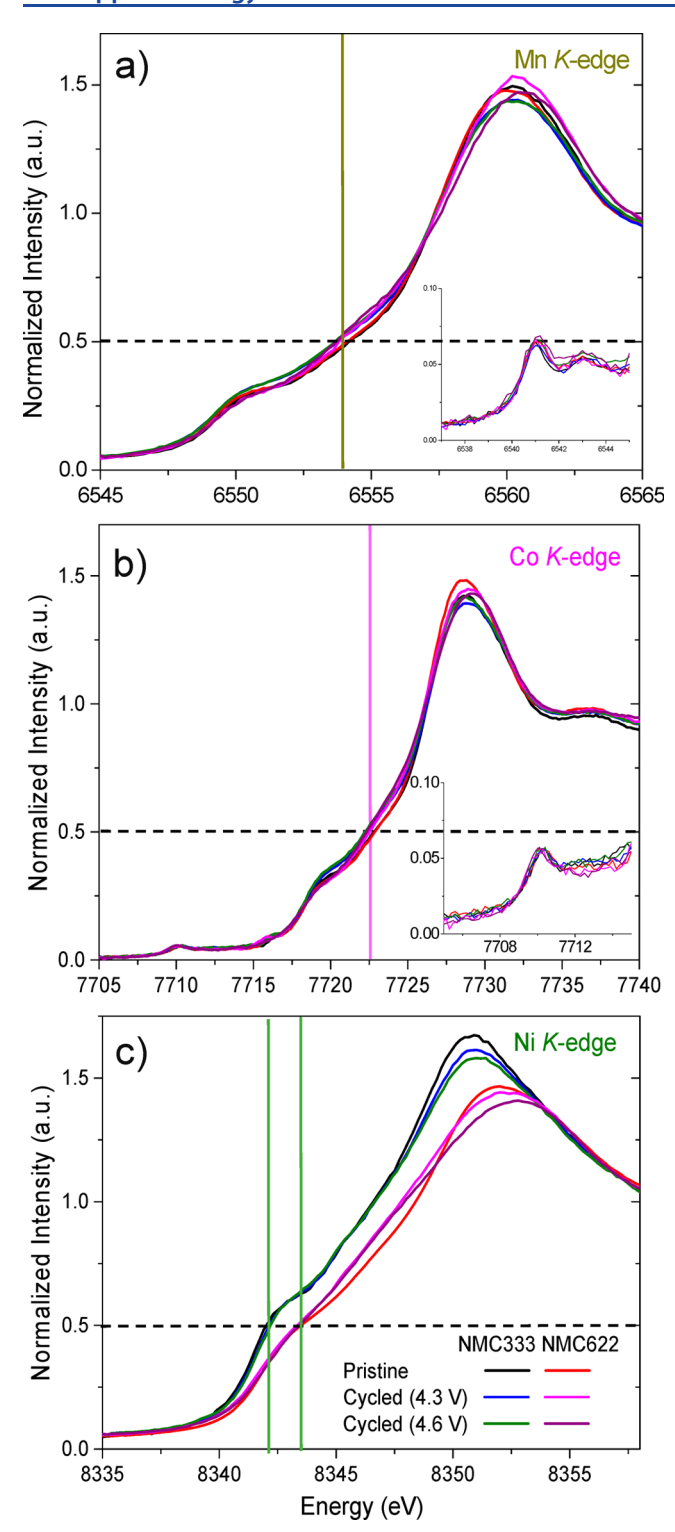


Figure 3. Hard XAS *K*-edge spectra of pristine and cycled NMC333 and NMC622 electrodes recovered after 100 cycles in 3.0–4.3 V and 3.0–4.6 V: (a) Mn, (b) Co, and (c) Ni.

ICP analysis is also consistent with the target compositions of both samples (Table S2).

The electrochemical performances of NMC333 and NMC622 crystal samples were evaluated by galvanostatically charging and discharging the half-cells at a rate of C/10 by using two voltage windows of 3.0–4.3 and 3.0–4.6 V. The evolution of the charge—discharge profile from the first cycle to

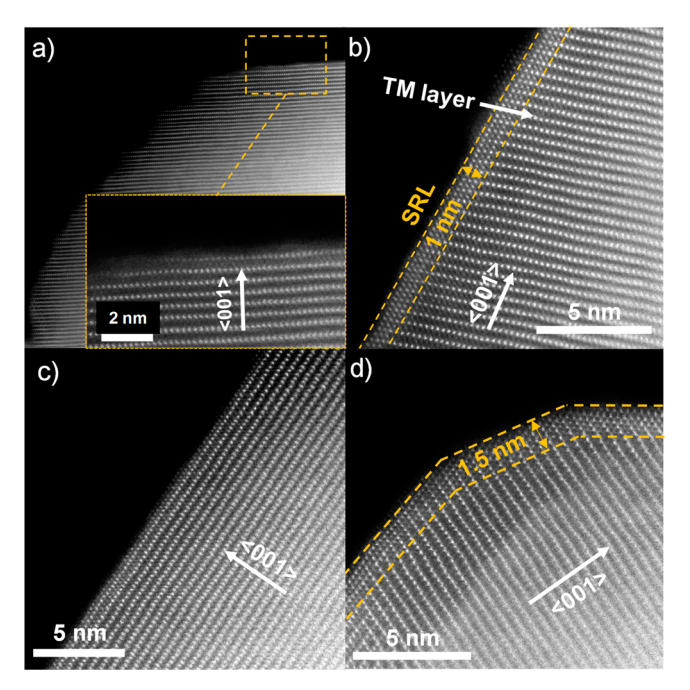


Figure 4. HAADF STEM imaging shows facet-dependent surface reconstruction on (a, b) pristine NMC333 and (c, d) pristine NMC622 particles. SRL was found on the non-(001) surface (b, d) while no SRL was observed on the (001) surface (a, c). The zone axis is [010] for all images.

the 100th cycle is plotted at an interval of 10 cycles and shown in Figure 2a—d. As might be expected, the capacity retention of the NMC333 was much better than that of the NMC622, especially when both electrodes were cycled between 3.0 and 4.3 V, where the Ni-rich NMC622 reaches a higher SOC. Cycling to a higher upper cutoff voltage of 4.6 V increases the initial discharge capacity but decreases the cycling stability of both samples, as shown in Figure 2e,f. This trend in capacity and stability trade-off is consistent with the previous reports on NMC materials. 42,43

After 100 cycles, the cathodes were recovered from the halfcells and subjected to hXAS analysis to probe changes in average TM oxidation states in the bulk of the sample. Figure 3 compares the K-edge spectra of Ni, Co, and Mn collected on the pristine and cycled NMC333 and NMC622 electrodes. The K-edge energy position of TMs at a normalized intensity of 0.5 is often used to index the oxidation state of TMs. A higher energy shift corresponds to an increase in TM oxidation state, and a lower energy shift corresponds to TM reduction. While Co and Mn are in +3 and +4 in both oxides, the calculated theoretical oxidation state of Ni in NMC333 and NMC622 is +2 and +2.67, respectively. The measured values in the pristine samples are consistent with these theoretical values. After cycling, either in the potential window of 3–4.3 V or 3-4.6 V, no obvious energy shift was observed on any TM K-edge energy positions, based on the normalized intensity of 0.5. This suggests negligible changes in TM chemical oxidation state in the bulk of the samples. However, it should be noted that the energy values at the normalized intensity of 0.5 does not reflect the subtle changes in chemical environment, particularly local structural changes due to distortion around the TM. 44,45 Careful comparison of the X-ray absorption nearedge structure (XANES) before and after cycling shows certain degree of spectral shape change in all three TMs, with the most

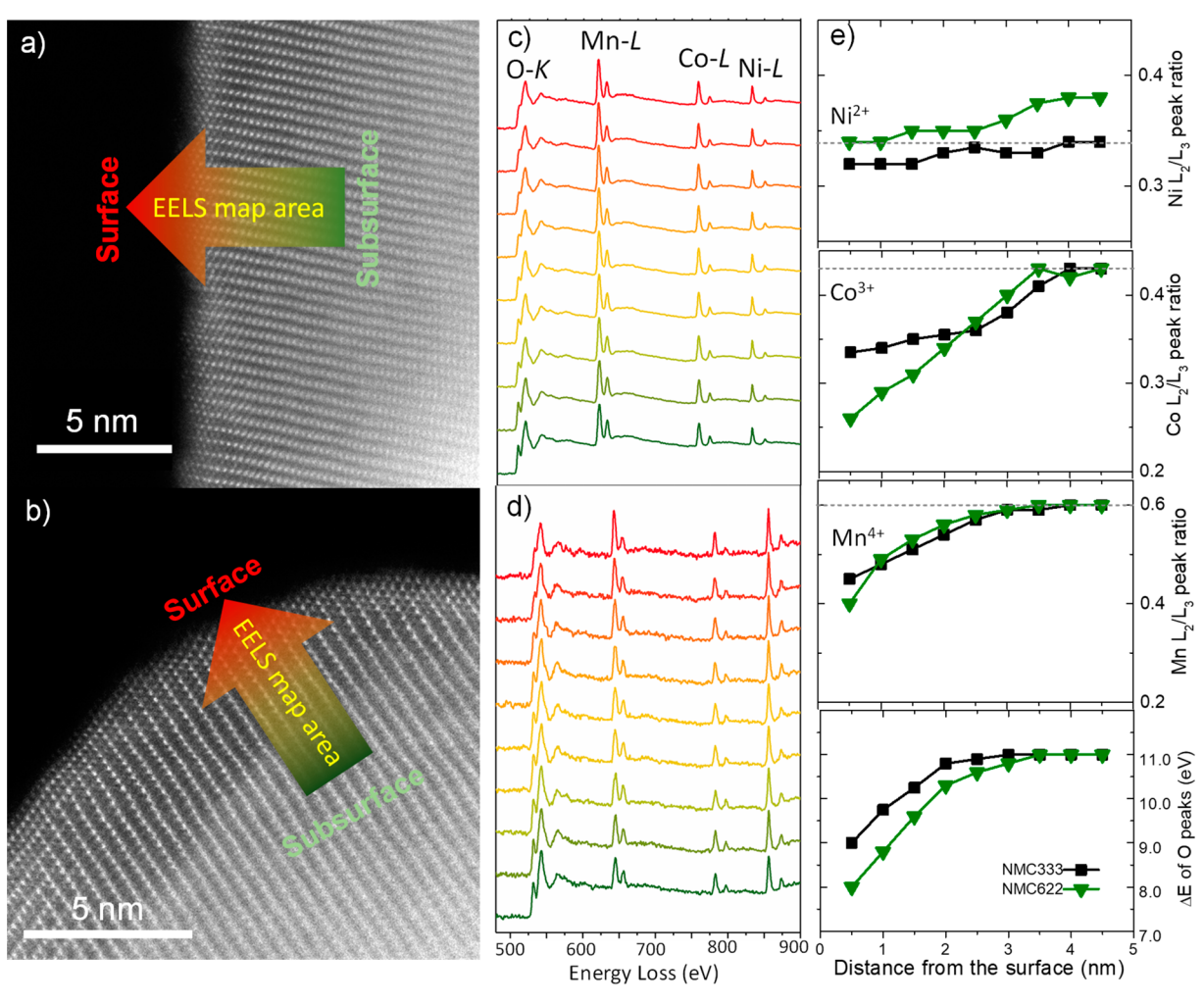


Figure 5. HAADF STEM imaging (a, b) and EELS data (c, d) collected on (a, c) NMC333 pristine particle and (b, d) NMC622 pristine particles. The step size from the surface to the bulk is 0.5 nm. (e) L_2/L_3 ratio of Ni, Co, and Mn as well as the energy difference between the prepeaks and main peaks of the O K-edge as a function of distance from the surface.

significant difference found in Mn K-edge spectra. The preedge peaks of Mn and Co (Figure 3, insets), on the other hand, remain similar before and after cycling. The spectral shape change in Ni K-edge is more substantial in cycled NMC622 than that in cycled NMC333, indicating enhanced structural distortion in the former with a higher Ni content. These subtle differences in spectral features are likely caused by some Li loss and the presence of vacant Li sites in crystal structure. At a discharge cutoff voltage of 3 V, it is conceivable that some Li sites remain inaccessible due to impedance rise with cycling.

3.2. NMC Surface Reconstruction. 3.2.1. Pristine NMCs. Layered structure with the $R\overline{3}m$ space group was further confirmed on the pristine particles by using atomic-resolution HAADF STEM imaging. As shown in Figure 4, the TM layers and Li layers are stacked along the c-axis. Cation disorder in NMC333 was negligible as bright spots were not observed in the dark Li slab regions. A small degree of cation disorder was seen in NMC622, consistent with the results of some cation mixing based on the Rietveld refinement (Figure S3). While no visible SRL was found on the (001) planes in both samples, where the surface is terminated by the Li-ion impermeable TM slabs (Figure 4a,c), a thin surface reconstruction layer with a thickness of ~1.0 and ~1.5 nm was found on the non-(001) surfaces of the pristine NMC333 (Figure 4a) and NMC622 (Figure 4c) particles, respectively. The nature of the surface

layer was further investigated by fast Fourier transform (FFT) processing of the STEM images taken in both side-view [010] zone axis (Figure S4a,c) and top-view [012] zone axis (Figure S4b,d). We note that to eliminate the ambiguities that arise from the fact that materials with different structures can give similar two-dimensional projections, three-dimensional structural information was obtained by imaging more than one zone axis. In both samples, it was found that the crystal structure of the surface layer is noticeably denser than that of the bulk, as some lithium sites were occupied by the TMs to form antisite defects, consistent with the previous reports.²² Depending on the surfaces examined, both "spinel-like" phase $(Fd\overline{3}m \text{ space})$ group, Figure S4b,c) and "rocksalt-type" phase (Fm3m space group, Figure S4a,d) were observed on NMC333 (Figure S4a,b) and NMC622 (Figure S4c,d). The transformation from the layered hexagonal structure to spinel is known to occur when 1/4 of the TM cations migrate into the Li sites, resulting a cubic symmetry that forces the Li cations into either the vacant TM octahedral or the tetrahedral sites. 12 In the rocksalt structure, TM cations also occupy the Li sites, but both TM and Li cations are intermixed in the same slabs. Further investigation on such SRL formation on the pristine NMC particles was performed by DFT calculations, and a manuscript is currently under preparation.

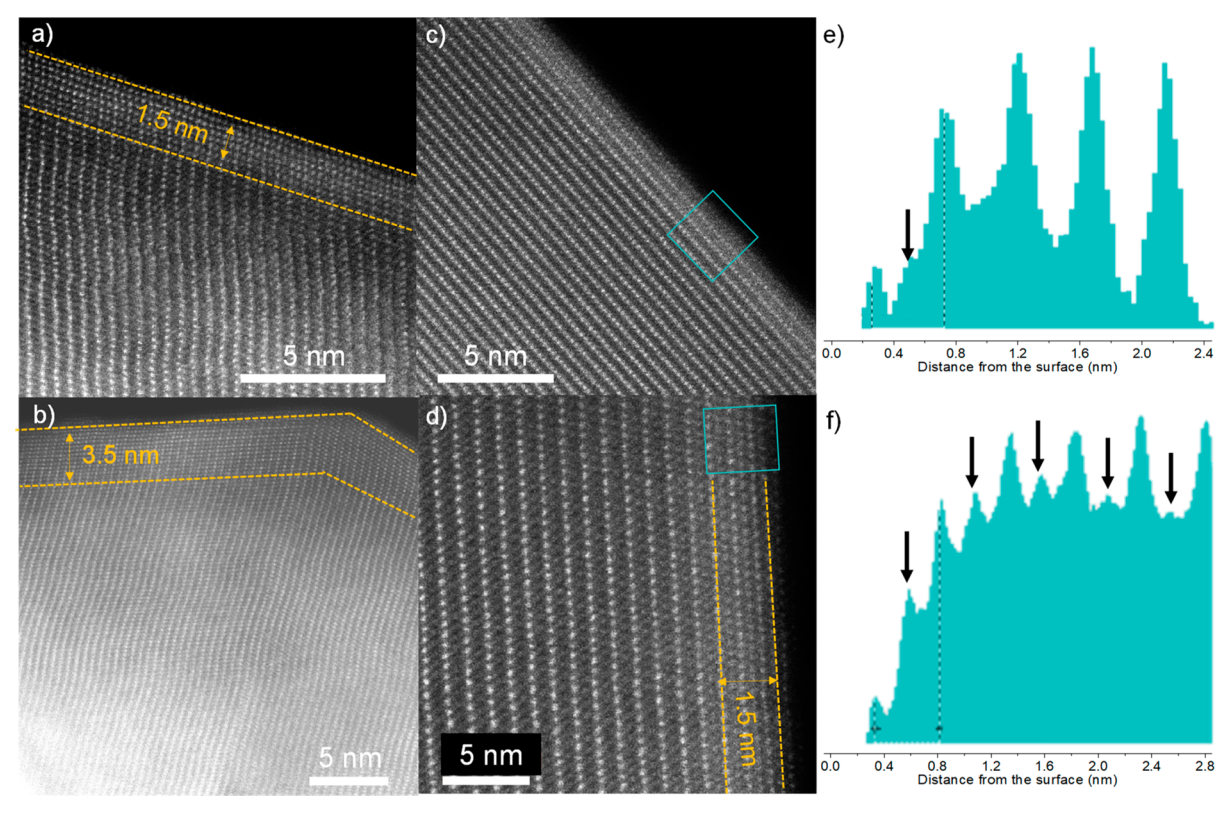


Figure 6. Atomic-resolution HAADF STEM images ([010] direction) show SRL formation on the non-(001) surface (a, b) and (001) surface (c, d) of cycled NMC333 (a, c) and NMC622 (b, d) platelet particles. (e) and (f) show the intensity profiles collected from the indicated area in NMC333 and NMC622, respectively. The zone axis is [010] for all images.

These results reveal that facet-dependent SRL formation occurs on the pristine NMC even before cycling. This is likely due to a difference in thermodynamic instability of the fresh surface during high-temperature annealing treatment. It is wellknown that high temperature promotes Li loss, and as a precaution, most solid-state synthesis uses an excess amount of Li precursors to compensate. 4,46 During the annealing process, a driving force exists for Li to leave the oxide lattice. Li loss can be expected on the non-(001) surface with open Li diffusion channels, 20 while the hindered (001) surface with alternating TM-O-Li layers largely prevents such a process. The vacant Li sites generated on the non-(001) surface are then available for occupancy by the antisite defects, mostly Ni cations due to the similar size of Ni²⁺ and Li⁺, resulting in surface densification or reconstruction of NMCs. Surface oxygen loss may also play a role in this process.

The SRL formation on the pristine NMC was also found to be composition-dependent. The thickness of SRL on NMC333 is ~1 nm while it increased to ~1.5 nm on NMC622. The difference is likely a result of overall better thermal stability in NMC333. 39,47 The higher Ni content in NMC622 also increases the probability of Ni migrating into the vacant Li sites, which is consistent with the results from the DFT calculations. Note that in this study the pristine NMC622 sample was prepared at a slightly lower temperature of 800 °C as compared to 850 °C used in NMC333 synthesis. This procedure was adopted to minimize cation exchange and optimize the layered structure in NMC622, following the recommendation in the previous reports. 48,49 One can expect even higher degree of surface reconstruction on NMC622 if the same synthesis temperature was used.

Further understanding on pristine surface SRL was achieved by using STEM/EELS analysis. Figures 5c and 5d show the EELS data collected in the non-(001) surface region of 5 nm (at a step size of 0.5 nm) in NMC333 and NMC622, as indicated on the STEM images in Figures 5a and 5b, respectively. Changes in O K-edge along with Mn, Ni, and Co L-edges were carefully examined, and the expanded view of the peaks are also shown in Figure S5. For NMC333, while Ni L-edge spectra remained nearly unchanged from the subsurface to the surface, a shift toward lower energy was observed on both Mn and Co L-edge spectra, suggesting a decrease in oxidation state toward the surface. 50-54 O K-edge EELS is known to be associated with the transition from O 1s to O 2p-TM 3d hybridized state, which is influenced by both TM oxidation states and the changes in O chemical environment. 16 The intensity reduction in the pre-edge peak at ~534 eV is consistent with the observed TM reduction on the surface. For NMC622, a low-energy shift was observed on all three TMs, including Ni. Figure 5e shows the L_2/L_3 ratio of each transition metal as well as the energy difference between the prepeaks and main peaks of the O K-edge as a function of distance from the surface. While L_2/L_3 ratio is often used to index the oxidation state of the investigated TM, 54 with a lower value corresponding to a lower oxidation state, the energy difference between the O K-edge peaks was recently used to quantify chemical changes in oxides. 55,56 It is evident that except Ni in NMC333 that remained at ~2+, TM reduction broadly occurred in the surface region of both oxides, along with a chemical gradient of increased reduction toward surface. Based on the energy difference between the O K-edge peaks, the estimated thickness of the reduction layer is ~2 and ~3 nm for NMC333 and NMC622, respectively. These values are higher

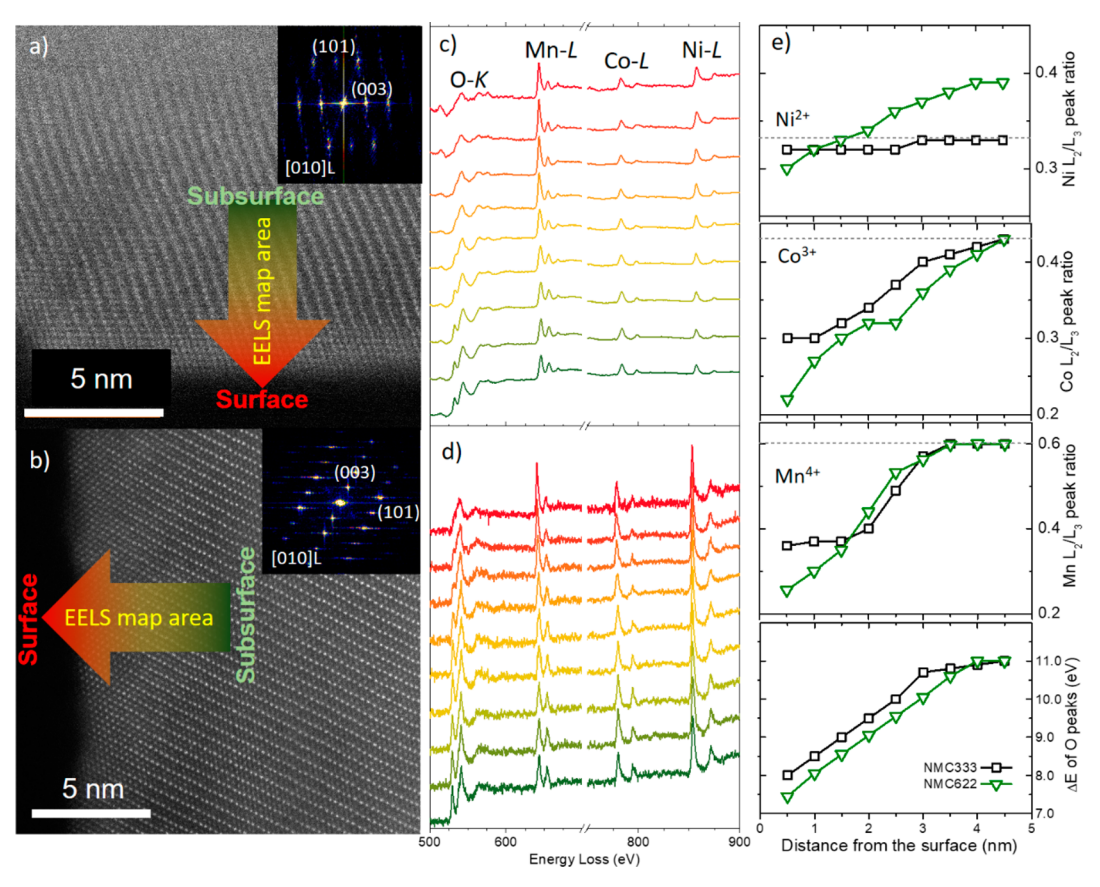


Figure 7. HAADF STEM imaging (a, b) and EELS spectra (c, d) collect on (a, c) cycled NMC333 particles and (b, d) cycled NMC622 particles. The step size from the surface to the bulk is 0.5 nm. (e) L_2/L_3 ratio of Ni, Co, and Mn as well as the energy difference between the prepeaks and main peaks of the O K-edge as a function of distance from the surface. The zone axis is [010], as shown in the STEM images. Insets of (a, b) show the FFT patterns from the entire area shown in the figures.

than the SRL thickness determined from STEM imaging, which are \sim 1 and \sim 1.5 nm, respectively. The results suggest that chemical changes not only occurs in the SRL, it also extends into the subsurface region beyond the distinct layer. The extent of TM reduction, however, is significantly higher in the SRL, consistent with the predominant secondary phase in the SRL. We note that due to the relatively coarse step size achievable in the EELS measurements (0.5 nm per step), the thickness values are only for estimation purposes. Nonetheless, our study not only provides particle-level confirmation on TM reduction in the SRL but also clearly reveals a transition region where the layered structure in the bulk was gradually replaced by the densified structure in the SRL.

A number of studies in the literature reported the presence of SRL with reduced TMs on cycled particles. 12,16,57,58 The changes have been attributed to the effect of cycling while the surface of pristine particles was not fully defined. We wish to emphasize that pristine samples obtained from solid-state synthesis are often secondary aggregates with a variety of crystalline orientations and built-in porosities and grain boundaries. As the facet- and composition-dependent nature of SRL is evident from our study, a careful investigation on structural and compositional inhomogeneities in the pristine sample is essential. To determine the real effect of cycling on chemical and structural changes, one has to ensure that the same crystalline orientation is examined for both pristine and cycled particles as well as the same composition is ensured throughout the particles.

3.2.2. Cycled NMCs. Post-mortem analysis was performed on the recovered cathode particles to evaluate structural and chemical changes caused by cycling. Figure 6 shows the atomic-resolution STEM images collected on NMC333 and NMC622 after 100 cycles between 3.0 and 4.6 V. It is evident that in both samples further SRL growth occurred during cycling, which also showed composition- and facet-dependent behavior. On the non-(001) surface, the thickness of the SRL increased from approximately 1 to 1.5 nm for NMC333 (Figure 6a) and 1.5 to 3.5 nm for NMC622 (Figure 6b). This corresponds to a net growth of 50% and ~135% after 100 cycles, nearly 3× faster in the higher Ni content NMC622 sample. Although no SRL was observed on the Li-impermeable (001) surface of pristine NMC333 or NMC622, cyclinginduced surface transformation was observed in both cases. As shown in Figures 6c and 6d, a thin SRL with ~3 atomic layers and ~ 1.5 nm was found on the (001) surface of the cycled NMC333 and NMC622, respectively. Surface densification was further evidenced by the derived intensity profiles shown in Figures 6e and 6f, revealing the migration and occupancy of TMs into the Li layer on the surface. Compared to the non-(001) surfaces, the growth of the SRL on the Li-impermeable (001) surface is significantly less severe, confirming the facetdependent nature of SRL growth due to cycling. Further FFT processing of the STEM images confirms the presence of both "spinel-like" and "rocksalt-type" structure in the densified surface layer. Factors influencing surface transformation during NMC cycling were recently investigated by HAADF-STEM

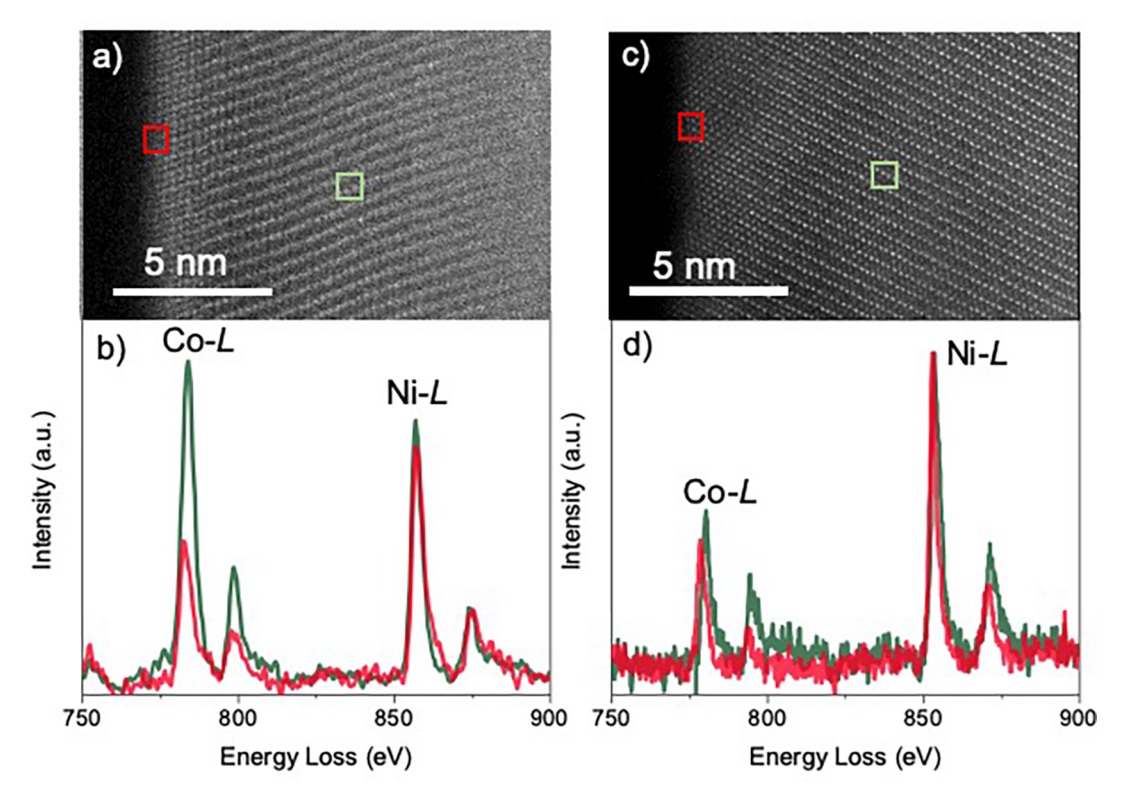


Figure 8. (a, c) HAADF STEM images and (b, d) EELS spectra of Co and Ni *L*-edge collected on the indicated areas on cycled NMC333 (a, b) and NMC622 (c, d) particles. The zone axis is [010] for all images.

imaging, and the results are being summarized in a separate paper.

Cycling-induced chemical changes in the SRL were evaluated by EELS analysis of O K-edge along with Mn, Ni, and Co L-edges. Figures 7c and 7d show the spectra collected in the indicated area in the STEM images from the non-(001) surface of NMC333 (Figure 7a) and NMC622 (Figure 7b), respectively. The expanded view of the peaks is also shown in Figure S6. Similar to the observation on the pristine samples, while Ni remained nearly unchanged at 2+ in the cycled NMC333, chemical reduction in Mn and Co was broadly detected in the surface region of both cycled samples. Figure 7e shows the L_2/L_3 ratio of each transition metal as well as the energy difference between the prepeaks and main peaks of the O K-edge as a function of distance from the surface. Compared to the pristine NMCs, more severe reduction and a thicker reduction layer with larger chemical gradient were found on the cycled particles. Based on the energy difference between the O K-edge peaks, the estimated thickness of the reduction layer with the chemical gradient increased from approximately 2 to 3 nm and 3 to 4 nm for NMC333 and NMC622, respectively. Similarly, the reduction layer is generally thicker than that of the SRL determined by STEM imaging, which were ~1.5 and 3.5 nm, respectively. The extent of TM reduction was significantly more severe in NMC622, confirming the role of chemical composition in surface stability. These results demonstrate that cycling not only promotes further growth of SRL but also modifies the chemical nature of the SRL.

While all three TMs were found in the SRL of the cycled NMC particles, a comparison of the EELS spectra collected on different regions reveals Ni segregation onto the surface. Figures 8b and 8d show Ni and Co *L*-edge spectra collected on

cycled NMC333 and NMC622, from the indicated areas in the STEM images shown in Figures 8a and 8c, respectively. For NMC333, the peak intensity ratio between Ni L-edge and Co L-edge is significantly higher on the top surface as compared to that in the subsurface region below ~5 nm, suggesting Ni enrichment in the SRL. Recent work based on first-principles calculations has shown that in NMCs nonpolar surfaces such as the (104) surface experience severe Ni segregation, which can facilitate the phase transformation from the layered to a denser crystal structure, such as spinel or rocksalt.³¹ Our results are consistent with the theory work, providing clear experimental evidence on the correlation between Ni migration and surface reconstruction. Surface TM segregation is largely composition-dependent. As shown in Figures 8c and 8d, the extent of surface Ni enrichment was much reduced in cycled NMC622. The exact role of chemical composition in surface TM segregation/enrichment is under further investigation.

3.2.3. Mechanisms for NMC Surface Reconstruction. As revealed by STEM imaging and EELS analysis, the SRLs on the pristine and cycled particles have similar nature, both showing chemical gradient as well as composition- and surface facet-dependent behavior. Previous studies have shown higher energy barrier in the migration of Mn or Co into the Li sites. S9,60 In our study, upon changing the chemical composition from NMC333 to NMC622, the Ni content was increased while both Mn and Co contents were reduced to the same degree. The observation of more severe surface reconstruction in the latter confirms that cation exchange and/or migration of Mn and/or Co are unlikely to occur at a meaningful level. The selective surface reconstruction therefore is likely a combined result of cation exchange (interplane) and cation migration (intraplane), particularly Li/Ni exchange and

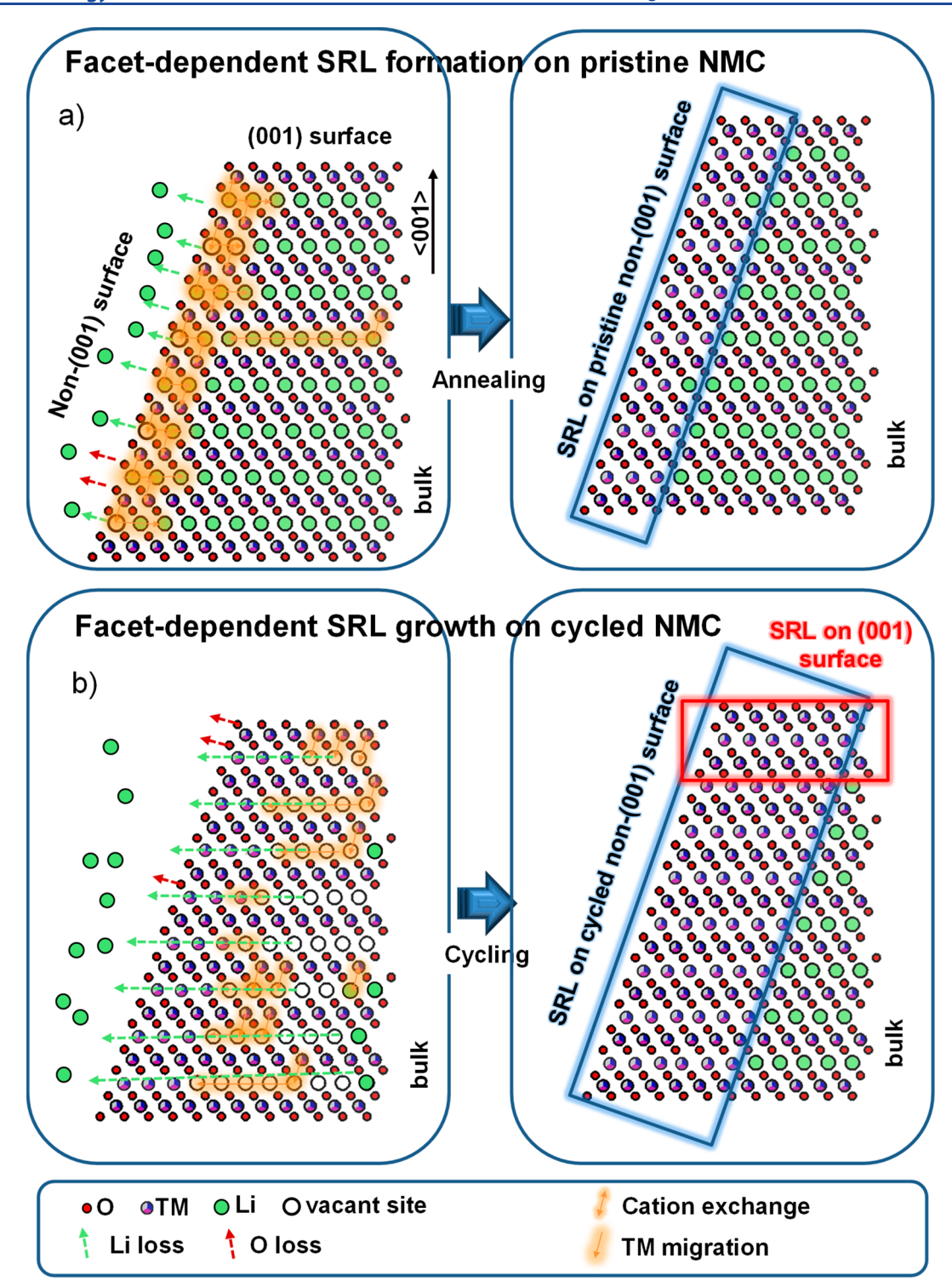


Figure 9. Schematics showing the processes that lead to SRL formation and growth on (a) pristine and (b) cycled NMC surfaces. Blue and red boxes highlight SRL on the non-(001) surface and (001) surface, respectively.

Ni migration due to the similar size of Ni and Li cations and the low energy barrier for Ni migration. ^{20,61} Li/Ni mixing and Ni migration processes are closely related to the Li loss from the lattice, which is facilitated by either high temperature during the synthesis ¹⁶ or high voltage during the electrochemical process. ⁵⁴ Figure 9 illustrates the proposed mechanism for SRL formation on the pristine particles (Figure 9a) and SRL growth on cycled particles (Figure 9b).

During the annealing process, both cation-ordering (which leads to formation of layered structure) and cation-disordering (which leads to formation of cation-mixed phase) processes take place simultaneously along with the formation of NMC crystals. As the processes compete with one another, controlling annealing time and annealing temperature are important to maximize the formation of layered structure while minimizing cation mixing in the bulk. Typically, unfavorable spinel or rocksalt structure forms when a longer reaction time

or a higher annealing temperature is used.² Even in the formed layered structure, prolonged heat exposure promotes Li loss on the non-(001) surface with open Li diffusion channels,²⁰ which is often accompanied by O loss from the lattice. The vacant Li sites are then available to be occupied by the antisite defects, mostly Ni cations due to the similar size of Ni²⁺ and Li⁺. The antisite Ni cations may migrate toward the surface region due to the low energy barrier of the intraplane transport,^{20,61} resulting in surface densification or reconstruction of the non-(001) NMC surface (Figure 9a). Depending on the extent of Li and/or O loss, both "spinel-like" and "rocksalt-type" phases can form. On the other hand, the hindered (001) surface with alternating TM-O-Li layers largely prevents such process, and therefore SRL formation is negligible on (001) surface of NMCs.

During electrochemical charge and discharge process, the driving force for the interplane cation exchange and intraplane TM transport is the repeated Li⁺ extraction/insertion process. During the charge, Li cations are removed from the Li slabs, starting from the surface to the bulk region. Delithiated NMCs are thermodynamically less stable than the pristine counterparts, and oxygen loss may also take place after extensive Li extraction at high voltages. 19,63 As a result, interplane Li/Ni cation site exchange broadly occurs within the NMC particle because of the relatively lower formation energy of Li/Ni exchange as compared to that of Li/Co or Li/Mn exchange. The subsequent intraplane migration of Li-site Ni toward the surface leads to Ni enrichment and SRL growth on the non-(001) surfaces (Figure 9b). It is evident that the presence of SRL on the pristine surface is insufficient in preventing further surface reconstruction during electrochemical cycling in the potential window of 3.0-4.6 V.

Formation of a thin SRL was also observed on the (001) surface of cycled NMCs, especially on NMC622. It is unclear whether surface reconstruction occurs on (001) surface due to O loss at high voltages. It is also possible that the observed SRL is simply a result of 2D projection of (001) with terraces and defects or the presence of a thicker SRL formed on the non-(001) surface (Figure 9b). Further studies are necessary to understand the formation and nature of SRL on cycled (001) surface.

4. CONCLUSIONS

In this study, we synthesized single-crystalline NMC particles with well-defined surface facets and utilized them to investigate the composition- and facet-dependent surface reconstruction behavior on both pristine and cycled particles. SRL selectively formed on the non-(001) surfaces whereas no SRL formation was found on the (001) surface of the pristine particles. A transition region with chemical gradient, in which the layered structure gradually densifies and eventually transforms into the SRL on the top surface, was clearly revealed. Cycling induces further SRL growth, which is also composition- and facetdependent. We propose that SRL formation during synthesis and SRL growth during electrochemical cycling share similar route causes, which are closely related to Li permeability of the facets, interplane Li/Ni cation exchange, and intraplane Ni migration. Non-(001) surfaces terminated with alternating TM-O-Li slabs and open Li diffusion channels are prone to Li loss and the subsequent Ni migration into the vacant Li sites. The resulting antisite Ni may further transport toward the surface via intraplane diffusion along the vacant Li channels/ slabs, leading to surface reconstruction and formation of SRL

enriched with Ni. These processes were facilitated by either the high-temperature annealing during the synthesis or the high-potential Li extraction/insertion during the electrochemical charge—discharge process. The insights obtained in this study provide guidance on the further design and development of better-performing oxide cathode materials in the future.

ASSOCIATED CONTENT

Supporting Information

The Supporting Information is available free of charge at https://pubs.acs.org/doi/10.1021/acsaem.0c00411.

List of Rietveld refinement parameters and elemental compositions from ICP measurements; EDX mapping collected under STEM imaging; crystallographic configurations of layered LiTMO₂; Rietveld refinement of synchrotron XRD patterns; HAADF STEM images and FFT analysis; EELS spectra of O K-edge, Mn L-edge, Co L-edge, and Ni L-edge collected on pristine and cycled samples (PDF)

AUTHOR INFORMATION

Corresponding Author

Guoying Chen — Energy Storage and Distributed Resources Division, Lawrence Berkeley National Laboratory, Berkeley, California 94720, United States; ⊙ orcid.org/0000-0002-3218-2609; Email: gchen@lbl.gov

Authors

Jian Zhu – Energy Storage and Distributed Resources Division, Lawrence Berkeley National Laboratory, Berkeley, California 94720, United States

Soroosh Sharifi-Asl — Department of Mechanical and Industrial Engineering, University of Illinois at Chicago, Chicago, Illinois 60607, United States; orcid.org/0000-0003-0441-9231

Juan C. Garcia – Chemical Sciences and Engineering Division, Argonne National Laboratory, Lemont, Illinois 60439, United States; orcid.org/0000-0002-5911-8850

Hakim H. Iddir — Chemical Sciences and Engineering Division, Argonne National Laboratory, Lemont, Illinois 60439, United States; Occid.org/0000-0001-5285-6474

Jason R. Croy − Chemical Sciences and Engineering Division, Argonne National Laboratory, Lemont, Illinois 60439, United States; © orcid.org/0000-0002-5839-3666

Reza Shahbazian-Yassar — Department of Mechanical and Industrial Engineering, University of Illinois at Chicago, Chicago, Illinois 60607, United States; orcid.org/0000-0002-7744-4780

Complete contact information is available at: https://pubs.acs.org/10.1021/acsaem.0c00411

Notes

The authors declare no competing financial interest.

ACKNOWLEDGMENTS

We thank Dr. Xiangyun Song at LBNL for assisting ICP measurements, Dr. Matthew Latimer and Dr. Erik Nelson at SSRL for assisting hard XAS measurements, and Dr. Dennis Nordlund for assisting soft XAS measurements. Use of the Stanford Synchrotron Radiation Lightsource, SLAC National Accelerator Laboratory is supported by the Office of Science, Office of Basic Energy Sciences of the U.S. Department of Energy under Contract DE-AC02-76SF00515. R. Shahbazian-

Yassar acknowledges the financial support from NSF award no. CBET-1805938. This work is supported by the Assistant Secretary for Energy Efficiency and Renewable Energy, Office of Vehicle Technologies of the U.S. Department of Energy under Contract DE-AC02-05CH11231.

REFERENCES

- (1) Radin, M. D.; Hy, S.; Sina, M.; Fang, C.; Liu, H.; Vinckeviciute, J.; Zhang, M.; Whittingham, M. S.; Meng, Y. S.; Van der Ven, A. Narrowing the Gap between Theoretical and Practical Capacities in Li-Ion Layered Oxide Cathode Materials. *Adv. Energy Mater.* **2017**, 7 (20), 1602888.
- (2) Xu, J.; Lin, F.; Doeff, M. M.; Tong, W. A review of Ni-based layered oxides for rechargeable Li-ion batteries. *J. Mater. Chem. A* **2017**, 5 (3), 874–901.
- (3) Li, W.; Song, B.; Manthiram, A. High-voltage positive electrode materials for lithium-ion batteries. *Chem. Soc. Rev.* **2017**, *46* (10), 3006–3059.
- (4) Zhao, J.; Zhang, W.; Huq, A.; Misture, S. T.; Zhang, B.; Guo, S.; Wu, L.; Zhu, Y.; Chen, Z.; Amine, K.; Pan, F.; Bai, J.; Wang, F. In Situ Probing and Synthetic Control of Cationic Ordering in Ni-Rich Layered Oxide Cathodes. *Adv. Energy Mater.* 2017, 7 (3), 1601266.
- (5) Schipper, F.; Erickson, E. M.; Erk, C.; Shin, J.-Y.; Chesneau, F. F.; Aurbach, D. Review—Recent Advances and Remaining Challenges for Lithium Ion Battery Cathodes: I. Nickel-Rich, LiNixCoyMnzO2. *J. Electrochem. Soc.* **2017**, *164* (1), A6220—A6228.
- (6) Jung, S.-K.; Gwon, H.; Hong, J.; Park, K.-Y.; Seo, D.-H.; Kim, H.; Hyun, J.; Yang, W.; Kang, K. Understanding the Degradation Mechanisms of LiNi0.5Co0.2Mn0.3O2 Cathode Material in Lithium Ion Batteries. *Adv. Energy Mater.* **2014**, *4* (1), 1300787.
- (7) Manthiram, A.; Song, B.; Li, W. A perspective on nickel-rich layered oxide cathodes for lithium-ion batteries. *Energy Storage Materials* **2017**, *6*, 125–139.
- (8) Myung, S.-T.; Maglia, F.; Park, K.-J.; Yoon, C. S.; Lamp, P.; Kim, S.-J.; Sun, Y.-K. Nickel-Rich Layered Cathode Materials for Automotive Lithium-Ion Batteries: Achievements and Perspectives. ACS Energy Lett. 2017, 2 (1), 196–223.
- (9) Zhao, W.; Zheng, J.; Zou, L.; Jia, H.; Liu, B.; Wang, H.; Engelhard, M. H.; Wang, C.; Xu, W.; Yang, Y.; Zhang, J.-G. High Voltage Operation of Ni-Rich NMC Cathodes Enabled by Stable Electrode/Electrolyte Interphases. *Adv. Energy Mater.* **2018**, 8 (19), 1800297.
- (10) Shkrob, I. A.; Gilbert, J. A.; Phillips, P. J.; Klie, R.; Haasch, R. T.; Bareno, J.; Abraham, D. P. Chemical Weathering of Layered Ni-Rich Oxide Electrode Materials: Evidence for Cation Exchange. *J. Electrochem. Soc.* 2017, 164 (7), A1489—A1498.
- (11) Zhang, X.; Belharouak, I.; Li, L.; Lei, Y.; Elam, J. W.; Nie, A.; Chen, X.; Yassar, R. S.; Axelbaum, R. L. Structural and Electrochemical Study of Al2O3 and TiO₂ Coated Li1.2Ni0.13Mn0.54-Co0.13O2 Cathode Material Using ALD. *Adv. Energy Mater.* **2013**, 3 (10), 1299–1307.
- (12) Kim, N. Y.; Yim, T.; Song, J. H.; Yu, J.-S.; Lee, Z. Microstructural study on degradation mechanism of layered LiNi0.6Co0.2Mn0.2O2 cathode materials by analytical transmission electron microscopy. *J. Power Sources* **2016**, *307*, 641–648.
- (13) Zhang, C.; Liu, M.; Pan, G.; Liu, S.; Liu, D.; Chen, C.; Su, J.; Huang, T.; Yu, A. Enhanced Electrochemical Performance of LiNi0.8Co0.1Mn0.1O2 Cathode for Lithium-Ion Batteries by Precursor Preoxidation. ACS Applied Energy Materials 2018, 1 (8), 4374–4384.
- (14) Ryu, H.-H.; Park, K.-J.; Yoon, C. S.; Sun, Y.-K. Capacity Fading of Ni-Rich Li[NixCoyMn1-x-y]O2 (0.6 $\le x \le$ 0.95) Cathodes for High-Energy-Density Lithium-Ion Batteries: Bulk or Surface Degradation? *Chem. Mater.* **2018**, 30 (3), 1155-1163.
- (15) Kim, J.; Cho, H.; Jeong, H. Y.; Ma, H.; Lee, J.; Hwang, J.; Park, M.; Cho, J. Self-Induced Concentration Gradient in Nickel-Rich Cathodes by Sacrificial Polymeric Bead Clusters for High-Energy Lithium-Ion Batteries. *Adv. Energy Mater.* **2017**, *7* (12), 1602559.

- (16) Lin, F.; Markus, I. M.; Nordlund, D.; Weng, T.-C.; Asta, M. D.; Xin, H. L.; Doeff, M. M. Surface reconstruction and chemical evolution of stoichiometric layered cathode materials for lithium-ion batteries. *Nat. Commun.* **2014**, *5*, 3529.
- (17) Li, J.; Liu, H.; Xia, J.; Cameron, A. R.; Nie, M.; Botton, G. A.; Dahn, J. R. The Impact of Electrolyte Additives and Upper Cut-off Voltage on the Formation of a Rocksalt Surface Layer in LiNi0.8Mn0.1Co0.1O2 Electrodes. *J. Electrochem. Soc.* **2017**, *164* (4), A655–A665.
- (18) Zou, L.; Liu, Z.; Zhao, W.; Jia, H.; Zheng, J.; Yang, Y.; Wang, G.; Zhang, J.-G.; Wang, C. Solid-Liquid Interfacial Reaction Trigged Propagation of Phase Transition from Surface into Bulk Lattice of Ni-Rich Layered Cathode. *Chem. Mater.* **2018**, *30* (20), 7016–7026.
- (19) Liu, H.; Harris, K. J.; Jiang, M.; Wu, Y.; Goward, G. R.; Botton, G. A. Unraveling the Rapid Performance Decay of Layered High-Energy Cathodes: From Nanoscale Degradation to Drastic Bulk Evolution. *ACS Nano* **2018**, *12* (3), 2708–2718.
- (20) Gu, M.; Belharouak, I.; Genc, A.; Wang, Z. G.; Wang, D. P.; Amine, K.; Gao, F.; Zhou, G. W.; Thevuthasan, S.; Baer, D. R.; Zhang, J. G.; Browning, N. D.; Liu, J.; Wang, C. M. Conflicting Roles of Nickel in Controlling Cathode Performance in Lithium Ion Batteries. *Nano Lett.* **2012**, *12* (10), 5186–5191.
- (21) Dixit, H.; Zhou, W.; Idrobo, J.-C.; Nanda, J.; Cooper, V. R. Facet-Dependent Disorder in Pristine High-Voltage Lithium—Manganese-Rich Cathode Material. *ACS Nano* **2014**, 8 (12), 12710–12716.
- (22) Yan, P. F.; Zheng, J. M.; Zheng, J. X.; Wang, Z. G.; Teng, G. F.; Kuppan, S.; Xiao, J.; Chen, G. Y.; Pan, F.; Zhang, J. G.; Wang, C. M. Ni and Co Segregations on Selective Surface Facets and Rational Design of Layered Lithium Transition-Metal Oxide Cathodes. *Adv. Energy Mater.* **2016**, *6* (9), 1502455.
- (23) Jarvis, K.; Wang, C. C.; Varela, M.; Unocic, R. R.; Manthiram, A.; Ferreira, P. J. Surface Reconstruction in Li-Rich Layered Oxides of Li-Ion Batteries. *Chem. Mater.* **2017**, 29 (18), 7668–7674.
- (24) Zhang, H.; May, B. M.; Serrano-Sevillano, J.; Casas-Cabanas, M.; Cabana, J.; Wang, C.; Zhou, G. Facet-Dependent Rock-Salt Reconstruction on the Surface of Layered Oxide Cathodes. *Chem. Mater.* **2018**, 30 (3), 692–699.
- (25) Zou, L.; Zhao, W.; Jia, H.; Zheng, J.; Li, L.; Abraham, D. P.; Chen, G.; Croy, J. R.; Zhang, J.-G.; Wang, C. The Role of Secondary Particle Structures in Surface Phase Transitions of Ni-Rich Cathodes. *Chem. Mater.* **2020**, 32, 2884.
- (26) Solé, V. A.; Papillon, E.; Cotte, M.; Walter, P.; Susini, J. A multiplatform code for the analysis of energy-dispersive X-ray fluorescence spectra. *Spectrochim. Acta, Part B* **2007**, *62* (1), 63–68.
- (27) Koczkur, K. M.; Mourdikoudis, S.; Polavarapu, L.; Skrabalak, S. E. Polyvinylpyrrolidone (PVP) in nanoparticle synthesis. *Dalton Trans.* **2015**, 44 (41), 17883–17905.
- (28) Chen, G. Y.; Hai, B.; Shukla, A. K.; Duncan, H. Impact of Initial Li Content on Kinetics and Stabilities of Layered Li1+x-(Ni0.33Mn0.33Co0.33)(1-x)O-2. *J. Electrochem. Soc.* **2012**, *159* (9), A1543—A1550.
- (29) Garcia, J. C.; Bareno, J.; Yan, J. H.; Chen, G. Y.; Hauser, A.; Croy, J. R.; Iddir, H. Surface Structure, Morphology, and Stability of Li(Ni1/3Mn1/3Co1/3)O-2 Cathode Material. *J. Phys. Chem. C* **2017**, 121 (15), 8290–8299.
- (30) Kramer, D.; Ceder, G. Tailoring the Morphology of LiCoO2: A First Principles Study. *Chem. Mater.* **2009**, *21* (16), 3799–3809.
- (31) Liang, C.; Longo, R. C.; Kong, F.; Zhang, C.; Nie, Y.; Zheng, Y.; Cho, K. Ab initio Study on Surface Segregation and Anisotropy of Ni-rich LiNi1–2yCoyMnyO2 (NCM) ($y \le 0.1$) Cathodes. *ACS Appl. Mater. Interfaces* **2018**, *10* (7), 6673–6680.
- (32) Zhu, J.; Chen, G. Single-crystal based studies for correlating the properties and high-voltage performance of Li[NixMnyCo1-x-y]O2 cathodes. *J. Mater. Chem. A* **2019**, *7* (10), 5463–5474.
- (33) Wang, F.; Xiao, S.; Chang, Z.; Yang, Y.; Wu, Y. Nanoporous LiNi1/3Co1/3Mn1/3O2 as an ultra-fast charge cathode material for aqueous rechargeable lithium batteries. *Chem. Commun.* **2013**, *49* (80), 9209–9211.

- (34) Huang, Z.-D.; Liu, X.-M.; Oh, S.-W.; Zhang, B.; Ma, P.-C.; Kim, J.-K. Microscopically porous, interconnected single crystal LiNi1/3Co1/3Mn1/3O2 cathode material for Lithium ion batteries. *J. Mater. Chem.* **2011**, 21 (29), 10777–10784.
- (35) Choi, J.; Manthiram, A. Crystal chemistry and electrochemical characterization of layered LiNi0.5-yCo0.5-yMn2yO2 and LiCo0.5-yMn0.5-yNi2yO2 ($0 \le 2y \le 1$) cathodes. *J. Power Sources* **2006**, *162* (1), *667*-*672*.
- (36) Lee, K.-S.; Myung, S.-T.; Amine, K.; Yashiro, H.; Sun, Y.-K. Structural and Electrochemical Properties of Layered Li [Ni1 -2x Co x Mn x] O2 (x = 0.1 0.3) Positive Electrode Materials for Li-Ion Batteries. *J. Electrochem. Soc.* **2007**, 154 (10), A971–A977.
- (37) Xiao, J.; Chernova, N. A.; Whittingham, M. S. Influence of Manganese Content on the Performance of LiNi0.9—yMnyCo0.1O2 (0.45 $\leq y \leq$ 0.60) as a Cathode Material for Li-Ion Batteries. *Chem. Mater.* **2010**, 22 (3), 1180–1185.
- (38) Min, K.; Kim, K.; Jung, C.; Seo, S.-W.; Song, Y. Y.; Lee, H. S.; Shin, J.; Cho, E. A comparative study of structural changes in lithium nickel cobalt manganese oxide as a function of Ni content during delithiation process. *J. Power Sources* **2016**, *315*, 111–119.
- (39) Sun, H.; Zhao, K. Electronic Structure and Comparative Properties of LiNixMnyCozO2 Cathode Materials. *J. Phys. Chem. C* **2017**, *121* (11), 6002–6010.
- (40) Sun, H.-H.; Manthiram, A. Impact of Microcrack Generation and Surface Degradation on a Nickel-Rich Layered Li-[Ni0.9Co0.05Mn0.05]O2 Cathode for Lithium-Ion Batteries. *Chem. Mater.* **2017**, 29 (19), 8486–8493.
- (41) Yoon, C. S.; Park, K.-J.; Kim, U.-H.; Kang, K. H.; Ryu, H.-H.; Sun, Y.-K. High-Energy Ni-Rich Li[NixCoyMn1-x-y]O2 Cathodes via Compositional Partitioning for Next-Generation Electric Vehicles. *Chem. Mater.* **2017**, *29* (24), 10436–10445.
- (42) Zheng, H.; Sun, Q.; Liu, G.; Song, X.; Battaglia, V. S. Correlation between dissolution behavior and electrochemical cycling performance for LiNi1/3Co1/3Mn1/3O2-based cells. *J. Power Sources* **2012**, 207, 134–140.
- (43) Kim, J.-H.; Park, K.-J.; Kim, S. J.; Yoon, C. S.; Sun, Y.-K. A method of increasing the energy density of layered Ni-rich Li[Ni1-2xCoxMnx]O2 cathodes (x = 0.05, 0.1, 0.2). *J. Mater. Chem. A* **2019**, 7 (6), 2694-2701.
- (44) Yu, X.; Lyu, Y.; Gu, L.; Wu, H.; Bak, S.-M.; Zhou, Y.; Amine, K.; Ehrlich, S. N.; Li, H.; Nam, K.-W.; Yang, X.-Q. Understanding the Rate Capability of High-Energy-Density Li-Rich Layered Li1.2Ni0.15-Co0.1Mn0.55O2 Cathode Materials. *Adv. Energy Mater.* **2014**, *4* (5), 1300950.
- (45) Croy, J. R.; Gallagher, K. G.; Balasubramanian, M.; Chen, Z. H.; Ren, Y.; Kim, D.; Kang, S. H.; Dees, D. W.; Thackeray, M. M. Examining Hysteresis in Composite xLi(2)MnO(3)center dot(1-x)LiMO2 Cathode Structures. *J. Phys. Chem. C* **2013**, *117* (13), 6525–6536.
- (46) Fu, C.; Li, G.; Luo, D.; Li, Q.; Fan, J.; Li, L. Nickel-Rich Layered Microspheres Cathodes: Lithium/Nickel Disordering and Electrochemical Performance. ACS Appl. Mater. Interfaces 2014, 6 (18), 15822–15831.
- (47) Bak, S.-M.; Hu, E.; Zhou, Y.; Yu, X.; Senanayake, S. D.; Cho, S.-J.; Kim, K.-B.; Chung, K. Y.; Yang, X.-Q.; Nam, K.-W. Structural Changes and Thermal Stability of Charged LiNixMnyCozO2 Cathode Materials Studied by Combined In Situ Time-Resolved XRD and Mass Spectroscopy. ACS Appl. Mater. Interfaces 2014, 6 (24), 22594–22601.
- (48) Sun, Y.-K.; Lee, D.-J.; Lee, Y. J.; Chen, Z.; Myung, S.-T. Cobalt-Free Nickel Rich Layered Oxide Cathodes for Lithium-Ion Batteries. *ACS Appl. Mater. Interfaces* **2013**, *5* (21), 11434–11440.
- (49) Ngala, J. K.; Chernova, N. A.; Ma, M.; Mamak, M.; Zavalij, P. Y.; Whittingham, M. S. The synthesis, characterization and electrochemical behavior of the layered LiNi0.4Mn0.4Co0.2O2 compound. *J. Mater. Chem.* **2004**, *14* (2), 214–220.
- (50) Tian, C.; Nordlund, D.; Xin, H. L.; Xu, Y.; Liu, Y.; Sokaras, D.; Lin, F.; Doeff, M. M. Depth-Dependent Redox Behavior of

- LiNi0.6Mn0.2Co0.2O2. J. Electrochem. Soc. 2018, 165 (3), A696–A704.
- (51) Lin, F.; Markus, I. M.; Doeff, M. M.; Xin, H. L. Chemical and Structural Stability of Lithium-Ion Battery Electrode Materials under Electron Beam. *Sci. Rep.* **2015**, *4*, 5694.
- (52) Mu, L.; Lin, R.; Xu, R.; Han, L.; Xia, S.; Sokaras, D.; Steiner, J. D.; Weng, T.-C.; Nordlund, D.; Doeff, M. M.; Liu, Y.; Zhao, K.; Xin, H. L.; Lin, F. Oxygen Release Induced Chemomechanical Breakdown of Layered Cathode Materials. *Nano Lett.* **2018**, *18* (5), 3241–3249.
- (53) Liu, H.; Bugnet, M.; Tessaro, M. Z.; Harris, K. J.; Dunham, M. J. R.; Jiang, M.; Goward, G. R.; Botton, G. A. Spatially resolved surface valence gradient and structural transformation of lithium transition metal oxides in lithium-ion batteries. *Phys. Chem. Chem. Phys.* **2016**, *18* (42), 29064–29075.
- (54) Kuppan, S.; Shukla, A. K.; Membreno, D.; Nordlund, D.; Chen, G. Revealing Anisotropic Spinel Formation on Pristine Li- and Mn-Rich Layered Oxide Surface and Its Impact on Cathode Performance. *Adv. Energy Mater.* **2017**, *7* (11), 1602010.
- (55) Croy, J. R.; O'Hanlon, D. C.; Sharifi-Asl, S.; Murphy, M.; Mane, A.; Lee, C.-W.; Trask, S. E.; Shahbazian-Yassar, R.; Balasubramanian, M. Insights on the Stabilization of Nickel-Rich Cathode Surfaces: Evidence of Inherent Instabilities in the Presence of Conformal Coatings. *Chem. Mater.* **2019**, *31* (11), 3891–3899.
- (56) Tornheim, A.; Sharifi-Asl, S.; Garcia, J. C.; Bareño, J.; Iddir, H.; Shahbazian-Yassar, R.; Zhang, Z. Effect of electrolyte composition on rock salt surface degradation in NMC cathodes during high-voltage potentiostatic holds. *Nano Energy* **2019**, *55*, 216–225.
- (57) Lin, F.; Nordlund, D.; Markus, I. M.; Weng, T.-C.; Xin, H. L.; Doeff, M. M. Profiling the nanoscale gradient in stoichiometric layered cathode particles for lithium-ion batteries. *Energy Environ. Sci.* **2014**, *7* (9), 3077–3085.
- (58) Lin, F.; Nordlund, D.; Pan, T.; Markus, I. M.; Weng, T.-C.; Xin, H. L.; Doeff, M. M. Influence of synthesis conditions on the surface passivation and electrochemical behavior of layered cathode materials. *J. Mater. Chem. A* **2014**, 2 (46), 19833–19840.
- (59) Yan, P. F.; Zheng, J. M.; Lv, D. P.; Wei, Y.; Zheng, J. X.; Wang, Z. G.; Kuppan, S.; Yu, J. G.; Luo, L. L.; Edwards, D.; Olszta, M.; Amine, K.; Liu, J.; Xiao, J.; Pan, F.; Chen, G. Y.; Zhang, J. G.; Wang, C. M. Atomic-Resolution Visualization of Distinctive Chemical Mixing Behavior of Ni, Co, and Mn with Li in Layered Lithium Transition-Metal Oxide Cathode Materials. *Chem. Mater.* 2015, 27 (15), 5393–5401.
- (60) Gao, A.; Sun, Y.; Zhang, Q.; Zheng, J.; Lu, X. Evolution of Ni/Li antisites under the phase transition of a layered LiNi1/3Co1/3Mn1/3O2 cathode. *J. Mater. Chem. A* **2020**, *8* (13), 6337–6348.
- (61) Lee, J. Y.; Kim, J. Y.; Cho, H. I.; Lee, C. H.; Kim, H. S.; Lee, S. U.; Prosa, T. J.; Larson, D. J.; Yu, T. H.; Ahn, J.-P. Three-dimensional evaluation of compositional and structural changes in cycled LiNi1/3Co1/3Mn1/3O2 by atom probe tomography. *J. Power Sources* **2018**, 379, 160–166.
- (62) Duan, Y.; Yang, L.; Zhang, M.-J.; Chen, Z.; Bai, J.; Amine, K.; Pan, F.; Wang, F. Insights into Li/Ni ordering and surface reconstruction during synthesis of Ni-rich layered oxides. *J. Mater. Chem. A* **2019**, 7 (2), 513–519.
- (63) Steiner, J. D.; Mu, L.; Walsh, J.; Rahman, M. M.; Zydlewski, B.; Michel, F. M.; Xin, H. L.; Nordlund, D.; Lin, F. Accelerated Evolution of Surface Chemistry Determined by Temperature and Cycling History in Nickel-Rich Layered Cathode Materials. *ACS Appl. Mater. Interfaces* **2018**, *10* (28), 23842–23850.